Site distribution of Fe²⁺ and Fe³⁺ in the axinite mineral group: New crystal-chemical formula

GIOVANNI B. ANDREOZZI,[1,*] SERGIO LUCCHESI,[1] GIORGIO GRAZIANI,[1] AND UMBERTO RUSSO[2]

[1]Dipartimento di Scienze della Terra, Università di Roma "La Sapienza", Piazzale Aldo, Moro 5, I-00185 Roma, Italy
[2]Dipartimento di Chimica Inorganica, Metallorganica e Analitica, Università di Padova, Via Loredan 4, I-35131 Padova, Italy

ABSTRACT

A set of nine samples of axinite, selected from 60 specimens from worldwide localities, were investigated by single-crystal X-ray diffraction, electron and ion microprobe, and ^{57}Fe Mössbauer spectroscopy. The selected samples cover the compositional join from almost pure ferroaxinite (80%) to pure manganaxinite (95%). A new crystal-chemical formula for the axinite mineral group is proposed: ^{VI}[X1 X2 Y Z1 Z2]$_2$^{IV}[T1 T2 T3 T4 T5]$_2$O$_{30}$(O$_w$OH$_{1-w}$)$_2$, where VI and IV are coordination numbers; X1 = Ca and very minor Na; X2 = Ca (in axinites) or Mn (in tinzenite); Y = Mn (in manganaxinite and tinzenite), Fe^{2+} (in ferroaxinite) or Mg (in magnesioaxinite), with minor Al and Fe^{3+}; Z1 = Al and Fe^{3+}; Z2 = Al; T1, T2, and T3 = Si; T4 = Si (and presumably very minor B); T5 = B and minor Si. Charge unbalance (w), due to heterovalent substitutions, is compensated for by O^{2-} → OH$^-$ substitution.

From ferroaxinite to manganaxinite, cell volume increases linearly from 568.70 to 573.60 Å^3. This is mainly due to an increase in the <Y-O> mean distance from 2.220 to 2.255 Å, which is directly related to the Mn population (up to 1.89 apfu). Fe^{3+} concentrations, as determined by ^{57}Fe Mössbauer spectra at 80 K, sub-regularly increase up to 0.27 apfu, and three cases are evidenced: (1) Fe^{3+} << Fe^{2+} (or no Fe^{3+}), in ferroaxinite; (2) Fe^{3+} < Fe^{2+}, in intermediate compositions, and (3) Fe^{3+} > Fe^{2+} (or only Fe^{3+}), in manganaxinite.

Chemical and structural data were co-processed via a computer minimization program to obtain the cation distribution scheme. Adopting the Hard-Sphere Model, empirical cation-oxygen distances were refined for every cation in the axinite structure. The results revealed that Fe^{2+} is ordered at the octahedral Y site (up to 1.61 apfu), whereas Fe^{3+} is ordered at the octahedral Z1 site (up to 0.26 apfu) and is almost absent in the smallest Z2 site, which is fully populated by Al. The observed Fe^{3+} partitioning is in agreement with the structural results, which show that the Z1 octahedron is always larger than Z2. Moreover, no Fe^{3+} is found at the tetrahedral sites, but Si → B substitution occurs at T5. The continuous Y dimensional increase from ferroaxinite to manganaxinite involves progressive enlargement of the edge-sharing Z1 octahedron. As a consequence, the ^{Z1}Fe^{3+} → ^{Z1}Al^{3+} substitution is structurally favored toward manganaxinite and points to a new end-member with the suggested name "ferri-manganaxinite."

INTRODUCTION

The axinite-group minerals, with general formula (Ca,Mn)$_4$ (Mn,Fe,Mg)$_2$Al$_4$B$_2$Si$_8$O$_{30}$(OH)$_2$, are complex borosilicates typically occurring in low- to medium-grade metamorphic environments (contact metamorphic, metasomatic, regional metamorphic) and Mn ore deposits. Axinites from different petrogenetic environments show great sensitivity to growth P-T-X-f_{O_2} conditions, as evidenced by a remarkable compositional flexibility (Pringle and Kawachi 1980; Ozaki 1972).

The axinite crystal structure, with $P\bar{1}$ symmetry, may be described as a sequence of alternating layers of tetrahedrally and octahedrally coordinated cations (Takéuchi et al. 1974). In the tetrahedral layer, two disilicate groups, each made up of Si1 and Si2 tetrahedra, are connected by the two B tetrahedra to form a six-membered ring. Two additional disilicate groups, made up of Si3 and Si4, share a corner with the B tetrahedra, forming a [B$_2$Si$_8$O$_{30}$] planar cluster. Slightly distorted octahedra, four occupied by Al (Al1 and Al2) and two filled by Mn, Fe, or

Mg [Fe(Mn)] share edges to form a six-membered finite chain: Fe(Mn)-Al1-Al2-Al2-Al1-Fe(Mn). These chains are laterally connected by highly distorted Ca-octahedra (Ca1 and Ca2) thus forming the octahedral layer. For a full description of the axinite structure see Andreozzi et al. (2000b).

The general formula and nomenclature now commonly accepted were proposed by Sanero and Gottardi (1968). For compositions with Ca close to 4 atoms per formula unit (apfu), the end-members are manganaxinite, ferroaxinite, and magnesioaxinite. The name tinzenite is used for a member of the group in which a Ca deficiency (2 < Ca < 4 apfu) is compensated by an excess of Mn, ordered at Ca2, the smaller of the two sites (Basso et al. 1973).

Structural refinements available in the literature (Basso et al. 1973; Takéuchi et al. 1974; Swinnea et al. 1981; Belokoneva et al. 1997; Andreozzi et al. 2000b) are too few to allow for systematic structural comparisons among the various members of the solid solution, so the crystal chemistry of the axinite mineral group is incompletely understood. Further difficulties arise in the quantitative measurement of boron and hydrogen (hence,

* E-Mail: gianni.andreozzi@uniroma1.it

most published chemical analyses are incomplete) and in the hypothesized intracrystalline disorder of some constituent cations (Pieczka and Kraczka 1994; Deer et al. 1986; Swinnea et al. 1981; Lumpkin and Ribbe 1979).

A structural formula for the axinite mineral group was proposed by Lumpkin and Ribbe (1979) and further revised by Andreozzi et al. (2000a) on the basis of the results of a multi-analytical study of 60 samples from 24 worldwide localities, covering the compositional field known for axinite so far. The results showed that B (instead of Al) is inversely related with Si, that Fe^{3+} principally substitutes for Al, but also for divalent cations, and that these heterovalent substitutions are balanced by an OH deficiency.

To fully describe the crystal chemistry of the axinite group, iron partitioning among octahedral and/or tetrahedral sites must be defined. In fact, differing distribution schemes for Fe^{2+} and Fe^{3+} have been proposed in the literature for various samples (Lumpkin and Ribbe 1979; Pieczka and Kraczka 1994; Fuchs et al. 1997; Zabinski et al. 2002), but their conclusions are conflicting. In the present study, nine axinite samples were investigated by X-ray diffraction, structural refinement (SREF), and ^{57}Fe Mössbauer spectroscopy (MS), with the aim of clarifying iron distribution mechanisms and related structural deformations.

METHODS

Analytical methods

Nine axinite fragments (Table 1) were selected from the batch previously analyzed (Andreozzi et al. 2000a) so as to be representative of the Fe-Mn join with low or no Mg (Fig. 1). Single-crystal diffraction data were collected with an automated four-circle Siemens $P4$ diffractometer at 296 K, with Mo$K\alpha$ radiation monochromatized by a graphite crystal (Table 2). Reduction of the 4116–4155 observed diffraction intensities was performed using the SHELXTL-PC program package after correction for absorption (semi-empirical), Lorentz and polarization effects. The final R values varied between 1.88 and 2.65%. Full details on the experimental procedures may be found in Andreozzi et al. (2000b). The cell parameters and selected interatomic distances are listed in Table 3. Final atomic coordinates, site scattering values, anisotropic displacement parameters, and observed and calculated structural factors for all samples may be obtained from the authors. For sample 47, the closest to the ideal manganaxinite end-member ever observed, final atomic coordinates, refined site scattering values reported as site mean atomic numbers (m.a.n.), and equivalent-isotropic displacement-parameters (B_{eq}) are listed in Table 4. Although the hydrogen coordinates were not satisfactorily refined, the approximate position was located at $x = 1.001(4)$, $y = 0.951(3)$, and $z = 0.627(3)$, with site occupancy fixed at the chemical content.

The chemical composition of the crystals (Table 5) was determined using electron and ion microprobe techniques, the latter for H and B quantitative measurements. Electron microprobe analyses (EMPA) were carried out with a Cameca SX 50 instrument equipped with five wavelength-dispersive spectrometers and a Link eXL energy-dispersive system. Data reduction and correction were made with ZAF-4/FLS software. Natural and synthetic standards used were: wollastonite (Si, Ca),

jadeite (Al, Na), periclase (Mg), fluor-phlogopite (F), magnetite (Fe), orthoclase (K), rutile (Ti), and metallic Mn, Cr, and Zn. Precision was within 1% for major elements and within 5% for minor elements. Hydrogen and boron contents were measured by Secondary Ion Mass Spectrometry (SIMS) with a Cameca IMS 4f ion microprobe. The procedure employed a static $^{16}O^-$ primary beam and the "energy filtering" technique; the empirical approach of working curves via calibration with standards was used to obtain the H_2O and B_2O_3 contents of the samples (Ottolini et al. 1993, 1995). Medium- to high-energy secondary ions and tourmaline and axinite reference samples were used to reduce the matrix effect on the measured quantities (Andreozzi et al. 2000a). Although the uncertainty of SIMS quantitative data is commonly considered to be no less than 10–15%, it was greatly improved by collecting independent data from the same samples, by determining the H_2O contents by thermogravimetric analysis, and by matching the SIMS data with the structural data, which allowed the uncertainty for B to be lowered to about 3%.

Iron speciation and distribution was determined by fitting ^{57}Fe Mössbauer spectra, collected at both 296 K (room temperature) and 80 K (liquid nitrogen temperature). Measurements were performed in a conventional constant acceleration spectrometer using a rhodium matrix ^{57}Co source (nominal strength 1.85 GBq). Absorbers were prepared by pressing finely ground samples with a powdered acrylic resin to self-supporting discs. Based on EMPA results, the Mössbauer absorbers of various samples were prepared so as to have about 2 mg Fe/cm^2, i.e., well below an absorber density at which thickness effects seriously influence Mössbauer results. Liquid nitrogen temperature measurements were performed using a continuous flow cryostat filled with liquid nitrogen, with temperature controlled to within ± 0.2 K. Data collection time was up to three days, to have good statistics. Spectral data for the velocity range –4 to +4 mm/s were recorded on a multichannel analyzer using 512 channels. After velocity calibration against a spectrum of high-purity α-Fe foil (25 μm thick) taken at room temperature, the raw data were folded to 256 channels. The spectra were fitted assuming Lorentzian line shape and using the commercial fitting program Recoil 1.04. The reduced χ^2 was used to evaluate statistical best fit, and uncertainties were calculated using the covariance matrix (Table 6). Errors are estimated at about ± 0.02 mm/s for center shift (CS), quadrupole splitting (QS), and line width (FWHM), and no less than ± 2% for doublet areas, mainly due to overlapping of subspectra in the central portion of the absorption spectrum.
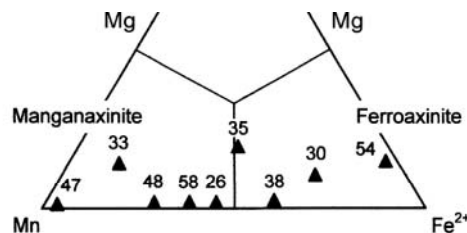

FIGURE 1. Mn-Fe^{2+}-Mg contents of axinite samples selected for this study. Symbol size corresponds to about $\pm 1\sigma$ of cation contents.

TABLE 1. Localities and sources of axinites used in this study

Sample no.	Locality	Source
26	Striegau, Slesia, Poland	MMR 17762/26
30	Rosebery, Tasmania, Australia	MMR 21020/30
33	Obira, Bungo, Japan	MMR 22055/33
35	S. Paolo Cervo, Biella, Italy	MMR 22293/35
38	Hajikami, Japan	MMR 22670/38
47	Graham, Arizona, US	Mr. R. Allori
48	Dalnegorsk, Vladivostok, Russia	Mr. R. Allori
54	Sri Lanka	Mr. M. de S. Jayasekera
58	Dalnegorsk, Vladivostock, Russia	Mr. L. Caserini

Note: MMR = Museum of Mineralogy, University of Rome "La Sapienza", Italy.

TABLE 2. Parameters for X-ray data collection

Unit-cell parameter determination	
Radiation (Å)	Mo$K\alpha_1$ 0.70930
Reflections used	13 (Friedel pairs on both + 2θ and -2θ)
Range (2θ)	83°–92°
Temperature (K)	296
Diffraction intensity collection	
Radiation (Å)	Mo$K\alpha$ 0.71073
Monochromator	High crystallinity graphite crystal
Range (2θ)	3–65°
Reciprocal space range	$-11 \leq h \leq 11$
	$-14 \leq k \leq 14$
	$0 \leq l \leq 14$
Scan method	ω
Scan range (2θ)	Fixed, 2.2°
Scan speed (2θ/min)	Variable, 2.93–29.30°
Temperature (K)	296
Data reduction	
Refinement	SHELXTL-PC
Corrections	Lorentz, Polarization
Absorption correction	Semi-empirical, 13 Ψ scans

TABLE 3. Structural parameters and selected mean bond-distances of Fe-Mn axinite samples

Ax no.	26	30	33	35	38	47	48	54	58
a (Å)	7.1654(3)	7.1601(4)	7.1703(4)	7.1636(4)	7.1635(4)	7.1849(4)	7.1765(4)	7.1479(4)	7.1653(4)
b (Å)	9.2004(5)	9.1988(5)	9.2031(5)	9.1994(5)	9.2044(5)	9.2152(5)	9.2132(5)	9.1962(5)	9.2053(5)
c (Å)	8.9665(4)	8.9608(4)	8.9666(4)	8.9634(4)	8.9622(4)	8.9765(4)	8.9707(4)	8.9576(4)	8.9655(4)
α (°)	91.831(4)	91.851(4)	91.803(4)	91.799(4)	91.834(4)	91.761(4)	91.791(4)	91.857(4)	91.772(4)
β (°)	98.143(3)	98.278(4)	98.120(4)	98.149(4)	98.213(4)	98.153(4)	98.136(4)	98.177(4)	98.107(4)
γ (°)	77.211(4)	77.354(4)	77.207(4)	77.271(4)	77.297(4)	77.150(4)	77.186(4)	77.359(4)	77.209(4)
V (Å³)	570.64(4)	569.88(5)	571.22(5)	570.36(5)	570.55(5)	573.60(5)	572.54(5)	568.70(5)	570.92(5)
Ext.	0.0048(2)	0.0015(2)	0.0050(2)	0.0020(2)	0.0030(2)	0.0010(1)	0.0021(2)	0.0259(4)	0.0049(2)
No. refl.	4134	4130	4136	4130	4130	4155	4146	4116	4135
R (%)	2.31	2.48	2.39	2.38	2.30	2.65	1.88	2.44	2.26
<T1-O>	1.623	1.622	1.622	1.622	1.623	1.623	1.623	1.624	1.623
<T2-O>	1.625	1.627	1.625	1.624	1.625	1.625	1.625	1.624	1.625
<T3-O>	1.629	1.630	1.628	1.629	1.630	1.629	1.629	1.630	1.629
<T4-O>	1.631	1.628	1.629	1.628	1.629	1.630	1.630	1.629	1.629
<T5-O>	1.493	1.487	1.487	1.490	1.486	1.487	1.487	1.487	1.486
<X1-O>	2.416	2.420	2.418	2.418	2.419	2.420	2.419	2.417	2.417
<X2-O>	2.391	2.389	2.393	2.392	2.390	2.391	2.393	2.392	2.392
<Y-O>	2.235	2.227	2.242	2.229	2.235	2.255	2.250	2.220	2.243
<Z1-O>	1.911	1.913	1.913	1.914	1.915	1.921	1.917	1.910	1.911
<Z2-O>	1.899	1.899	1.900	1.901	1.900	1.903	1.901	1.898	1.900

Notes: Ext. = Isotropic extinction coefficient; No. refl. = Number of observed reflections; $R = (\Sigma|F_{obs} - F_{calc}|)/(\Sigma F_{obs})$.

The Fe total content was measured as FeO_{tot} by EMPA, and actual Fe^{2+} and Fe^{3+} contents were obtained by matching Fe^{2+}/Fe^{3+} ratios measured by MS with the EMPA data, thus obtaining cation frequencies (Table 5). The contents of Fe^{2+} and Fe^{3+} were also calculated by charge balance from EMPA data on a stoichiometric basis. This procedure was possible because B and H were analyzed by SIMS and, as indicated by SREF, there was no evidence of cation vacancies (Andreozzi 1997). The results are listed in Table 5, and confirm the high reliability of the chemical data set, because calculated Fe^{2+} and Fe^{3+} contents very satisfactorily matched those measured by MS ($r = 0.92$).

Determination of cation distribution

In order to obtain the actual cation distribution over the octahedral sites, chemical and structural data from refined samples were co-processed using a computer minimization program (James and Roos 1975) specifically adapted for axinite. This approach, which is identical to that successfully adopted for other minerals (Lavina et al. 2002; Bosi and Lucchesi 2004), simultaneously takes into account both structural and chemical data and reproduces observed parameters by optimizing cation distribution. Differences between observed and calculated parameters were minimized using the "chi-square" function:

$$F(X_i) = \frac{1}{n} \sum_{j=1}^{n} \left(\frac{O_j - C_j(X_i)}{\sigma_j} \right)^2 \tag{1}$$

where O_j is the observed quantity, σ_j its standard deviation, X_i the variables, i.e., cation fractions in structural sites, and $C_j(X_i)$ the same quantity as O_j calculated by means of X_i parameters.

The nO_j ($n = 18$) quantities taken into account were: mean bond distances, m.a.n. and full occupancy of octahedral sites, chemical composition, and constraints imposed by crystal chemistry (total charges). Several minimization cycles of Equation 1 up to convergence were performed using a home-developed calculation routine. Bond distances were calculated, within the framework of the ionic model (Burnham 1990), as the linear contribution of each cation site population multiplied by its specific site bond-distance. These empiric cation-O atom distances were refined for each cation in every site (Table 7).

The following assumptions were made during minimization: (1) in case of Ca deficiency, an adequate amount of Mn^{2+} was fixed at Ca2 (Basso et al. 1973); (2) Mg, Zn, and Ti were fixed at the Fe(Mn) site, given their low quantities and following their general preference (Lumpkin and Ribbe 1979; Grew 1996; Andreozzi et al. 2000a); specific bond distances were taken from Andreozzi et al. (2000b) for Mg, and calculated from Shannon (1976) for Zn and Ti. On the basis of previous studies, the following sites were not included in the minimization because their composition was already constrained by chemical results: (1) the Si1-Si4 sites, fully populated by Si (and rarely by very minor B); (2) the B site, populated by B and minor Si; (3) the Ca1 site, populated only by Ca (and rarely by very minor Na).

Final $F(X_i)$ values ranging from 0.8 to 2.0 were obtained, confirming that chemical and structural parameters were reproduced, on average, within experimental error (Table 7), and hence that the corresponding cation distributions are highly reliable.

TABLE 4. Fractional atomic coordinates, mean atomic number (m.a.n) and equivalent displacement parameters of manganaxinite, sample 47

Position	x	y	z	m.a.n.	$U_{eq.}$
T1	0.21431(6)	0.45019(5)	0.23727(5)	13.96(4)	0.00472(12)
T2	0.21933(6)	0.27500(5)	0.52453(5)	13.91(4)	0.00401(12)
T3	0.70072(6)	0.25369(5)	0.01152(5)	13.89(4)	0.00478(12)
T4	0.64055(6)	0.01901(5)	0.23013(5)	13.96(4)	0.00447(12)
T5	0.46165(22)	0.63523(18)	0.28647(18)	4.61(4)	0.00132(43)
X1	0.74611(4)	0.34774(3)	0.39587(4)	19.78(4)	0.00775(9)
X2	0.18328(5)	0.10062(3)	0.08379(4)	20.03(4)	0.00857(9)
Y	0.76934(3)	0.58917(3)	0.11157(3)	24.73(4)	0.00797(7)
Z1	0.05275(6)	0.80181(4)	0.25422(4)	14.70(4)	0.00412(12)
Z2	0.35213(6)	0.93654(5)	0.42153(5)	13.15(4)	0.00422(13)
O1	0.05970(16)	0.60338(12)	0.18974(13)	8	0.00692(29)
O2	0.23487(17)	0.33740(13)	0.10084(13)	8	0.00916(31)
O3	0.42142(15)	0.48736(12)	0.31412(13)	8	0.00673(29)
O4	0.13711(17)	0.37590(13)	0.37345(13)	8	0.00980(32)
O5	0.02186(15)	0.24271(13)	0.56344(12)	8	0.00655(29)
O6	0.32635(15)	0.37826(12)	0.64732(12)	8	0.00614(29)
O7	0.38006(15)	0.12749(12)	0.49598(12)	8	0.00509(28)
O8	0.54054(15)	0.34368(12)	0.87721(12)	8	0.00664(29)
O9	0.87760(15)	0.15216(12)	0.93434(12)	8	0.00660(29)
O10	0.77047(17)	0.36264(13)	0.13966(13)	8	0.00890(31)
O11	0.60365(17)	0.13357(13)	0.08602(13)	8	0.00924(31)
O12	0.43632(15)	0.98193(12)	0.24413(12)	8	0.00651(29)
O13	0.71944(15)	0.09975(12)	0.38340(12)	8	0.00596(29)
O14	0.79302(16)	0.87344(13)	0.17787(13)	8	0.00753(29)
O15	0.32625(15)	0.74656(12)	0.35564(12)	8	0.00531(28)
O16	0.09696(15)	0.99702(12)	0.32332(12)	8	0.00668(29)

RESULTS

Chemical composition

The chemical compositions of the samples are almost evenly distributed along the known Mn-Fe axinite solid-solution join (Fig. 1). Measured contents of Fe^{2+} range from 0.11 to 1.56 apfu, i.e., increasing from samples 47 to 54. Sample 47 is in fact very close to the manganaxinite end-member (95%), and sample 54 corresponds to an 80% ferroaxinite, among the highest known so far. Mg contents either plot close to zero or around 0.30 apfu. The Fe^{3+} contents show behavior opposite of Fe^{2+}, ranging from 0.27 to 0.04 apfu, with a poorly regular decrease from manganaxinite to ferroaxinite (Table 5). From these results, three different Fe^{3+}/Fe^{2+} relationships are evident: (1) $Fe^{3+} > Fe^{2+}$ (or only Fe^{3+}) in manganaxinite, sample 47; (2) $Fe^{3+} < Fe^{2+}$ in

TABLE 5. Chemical composition of Fe-Mn axinite samples (wt%) from multi-analytical approach

Ax no.	26[a]	30	33[b]	35[c]	38	47	48[d]	54[e]	58[f]
SiO_2	42.4(2)	41.7(4)	42.9(3)	42.8(2)	42.3(1)	41.8(2)	42.3(2)	42.1(4)	42.8(5)
B_2O_3*	5.7(1)	6.3(2)	6.0(2)	6.0(2)	6.1(2)	6.0(2)	6.1	6.3(2)	6.1(2)
Al_2O_3	17.6(2)	17.5(2)	17.8(2)	17.3(2)	17.8(2)	16.7(3)	16.7(1)	17.7(2)	18.2(2)
FeO_{tot}	6.1(3)	9.4(1)	2.12(7)	6.5(3)	8.7(4)	2.3(4)	5.0(6)	10.60(7)	5.5(9)
MgO	0.15(2)	0.74(3)	1.07(6)	1.4(1)	0.19(4)	0.02(2)	0.13(5)	1.07(4)	0.14(3)
MnO	6.8(4)	2.88(5)	9.7(5)	5.1(4)	4.7(2)	12.5(2)	9.2(5)	0.4(1)	7.8(9)
CaO	19.1(2)	19.06(9)	19.27(9)	19.28(8)	18.9(2)	18.9(1)	19.2(1)	19.38(7)	19.4(3)
H_2O†	1.5(1)	1.3(1)	1.6(1)	1.6(1)	1.4(1)	1.4(1)	1.6(1)	1.6(1)	1.5(1)
Tot	99.5	98.9	100.5	100.0	100.1	99.6	100.4	99.2	101.4
FeO‡	5.4(1)	8.3(2)	1.87(4)	5.5(1)	7.2(2)	0.68(5)	4.0(1)	9.9(2)	4.5(1)
Fe_2O_3‡	0.7(1)	1.3(2)	0.28(4)	1.1(1)	1.6(2)	1.85(5)	1.1(1)	0.8(2)	1.1(1)
FeO§	5.73	6.47	2.04	6.33	7.34	0.00	3.75	10.60	4.82
Fe_2O_3§	0.36	3.29	0.09	0.19	1.51	2.60	1.36	0.00	0.76
	Number of ions on the basis of 32 (O,OH)								
Si	8.09(2)	7.98(2)	8.05(1)	8.04(2)	8.01(1)	8.02(3)	8.03(2)	7.97(2)	8.00(2)
B	1.88(5)	2.07(5)	1.94(5)	1.94(5)	1.99(5)	1.99(5)	2.00	2.06(5)	1.95(5)
Al	3.97(4)	3.94(2)	3.93(3)	3.84(4)	3.97(4)	3.77(6)	3.74(2)	3.94(1)	4.01(2)
Fe^{3+}	0.11(2)	0.18(3)	0.04(1)	0.15(2)	0.23(3)	0.27(1)	0.15(2)	0.12(3)	0.16(2)
Fe^{2+}	0.86(2)	1.33(3)	0.29(1)	0.87(3)	1.14(3)	0.11(1)	0.64(2)	1.56(3)	0.71(2)
Mg	0.04(1)	0.21(1)	0.30(2)	0.40(4)	0.05(1)	0.01(1)	0.04(1)	0.30(1)	0.04(1)
Mn	1.09(4)	0.47(3)	1.55(4)	0.81(4)	0.75(1)	2.03(2)	1.48(9)	0.06(2)	1.24(16)
Ca	3.92(3)	3.91(2)	3.87(2)	3.88(2)	3.84(3)	3.88(3)	3.91(2)	3.93(3)	3.88(2)
Tot	19.98[a]	20.09	19.99[b]	19.96[c]	19.98	20.07	20.01[d]	19.96[e]	20.00[f]
OH	1.9(1)	1.7(1)	2.0(1)	2.0(1)	1.8(1)	1.8(1)	2.0(1)	2.0(1)	1.9(1)

Notes: Standard deviations (1σ) are reported in brackets. F, K and Cr were analyzed but not detected; [a]Includes Zn 0.02, [b]includes Zn 0.02, [c]includes Ti 0.03, [d]includes Zn 0.03, [e]includes Zn 0.01 and Na 0.01, [f]includes Zn 0.01 (all values in apfu).
* From SIMS (except sample 48, data not available, B according to stoichiometry).
† From SIMS.
‡ From Mössbauer spectroscopy.
§ From stoichiometry (reported for comparison only, not used for ion calculation).

intermediate compositions, and (3) $Fe^{3+} \ll Fe^{2+}$ (or no Fe^{3+}) in ferroaxinite, sample 54. Notably, in case (1), which has never previously been observed, the high Fe^{3+} content is matched by a comparably low Al content (Table 5), suggesting the homovalent substitution $Fe^{3+} \rightarrow Al^{3+}$.

With manganaxinite $Ca_4Mn_2Al_4B_2Si_8O_{30}(OH)_2$ as the additive component, the Fe^{2+} and Mg substitutions are described by the $Fe^{2+}Mn_{-1}$ and $MgMn_{-1}$ substitutional vectors, respectively. Calcium deficiencies (up to 0.16 apfu) are compensated by excess Mn^{2+}, and the vector $MnCa_{-1}$ describes the tinzenite component. In almost all samples, B is below stoichiometry and is substituted by Si. Charge unbalance is compensated by $O^{2-} \rightarrow OH^-$ exchange, according to the mechanism $SiO(BOH)_{-1}$, previously described in Andreozzi et al. (2000a). In samples 30 and 54, however, a small B excess is matched by a Si deficiency, which may indicate a $B \rightarrow Si$ substitution.

[57]Fe Mössbauer spectra

Room temperature [57]Fe Mössbauer spectra of axinite samples show continuous variations from ferroaxinite to manganaxinite (Fig. 2). Following the existing literature, most of the spectra were interpreted with only two doublets, one for ferrous and the other for ferric iron. A few, however, required three subspectra, two for Fe^{2+} and one for Fe^{3+}. In only one case (sample 54) was a single doublet enough to reproduce the spectrum. Fe^{2+} and Fe^{3+} contents were quantified by analyzing doublet areas of the liquid nitrogen temperature spectra to achieve the highest

accuracy. In fact, $f(Fe^{2+})$ and $f(Fe^{3+})$ Mössbauer fractions may assume different values at room temperature, but are very close to each other at liquid nitrogen temperature (Eeckhout and De Grave 2003, and references therein). The hyperfine parameters are listed in Table 6.
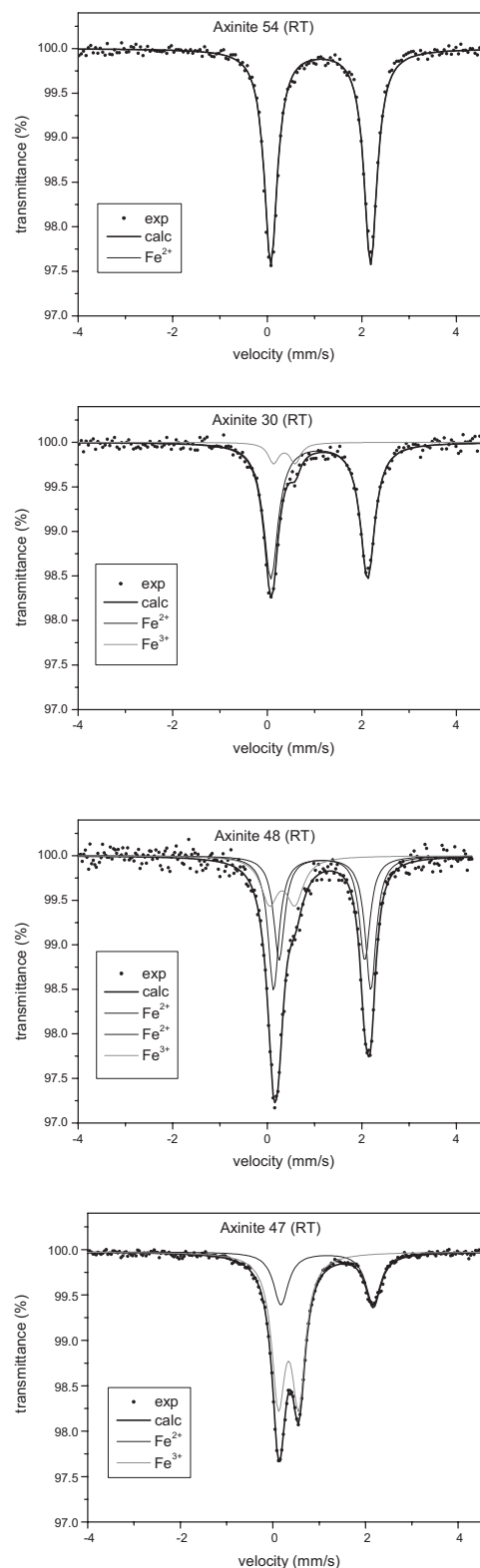
As mentioned above, the room temperature spectrum of ferroaxinite 54 shows only one Fe^{2+} doublet, with CS = 1.13 mm/s and QS = 2.11 mm/s, which indicates 100% Fe^{2+} in octahedral coordination. The spectrum collected at liquid nitrogen temperature is better resolved and shows a main doublet for Fe^{2+} (CS 1.25 and QS 2.58 mm/s) and a smaller inner doublet, attributed to Fe^{3+} in octahedral coordination (CS 0.47, QS 0.69 mm/s). The intensities measured for the two doublets are 93% (Fe^{2+}) and 7% (Fe^{3+}) with respect to total iron. Samples with intermediate composition exhibit more complex spectra that can be fitted with two or three doublets, as in the case of samples 30 and 48, respectively (Fig. 2). At room temperature, the main outer doublets have CS values from 1.06 to 1.17 mm/s and QS values from 1.81 to 2.18 mm/s, and were therefore attributed to octahedrally coordinated Fe^{2+}. Minor inner doublets have CS values between 0.30–0.45 mm/s and QS values from 0.27 to 0.62 mm/s and are attributed to octahedrally coordinated Fe^{3+}. At liquid nitrogen temperature, most of the spectra show better resolution, except for samples 26 and 58, which show an anomalously large line-width for the ferric component. This feature may be explained by the presence of two doublets due to Fe^{3+} located in two different octahedral environments. An extra doublet was tentatively added, but un-

TABLE 6. Mössbauer parameters and site attribution for Fe-Mn axinite samples

Sample	Temperature	CS (mm/s)	QS (mm/s)	FWHM (mm/s)	Intensity (%)	Attribution
26	RT	1.17	2.08	0.34	84	Oct. Fe^{2+}
		0.31	0.50	0.65	16	Oct. Fe^{3+}
	80 K	1.27	2.79	0.36	26	Oct. Fe^{2+}
		1.25	2.38	0.45	63	Oct. Fe^{2+}
		0.37	0.26	0.65	11	Oct. Fe^{3+}
30	RT	1.10	2.05	0.37	90	Oct. Fe^{2+}
		0.36	0.46	0.27	10	Oct. Fe^{3+}
	80 K	1.26	2.57	0.33	88	Oct. Fe^{2+}
		0.47	0.57	0.40	12	Oct. Fe^{3+}
33	RT	1.16	2.05	0.34	87	Oct. Fe^{2+}
		0.33	0.51	0.37	13	Oct. Fe^{3+}
	80 K	1.28	2.54	0.32	88	Oct. Fe^{2+}
		0.45	0.52	0.27	12	Oct. Fe^{3+}
35	RT	1.15	2.07	0.35	80	Oct. Fe^{2+}
		0.30	0.62	0.42	20	Oct. Fe^{3+}
	80 K	1.25	2.53	0.43	85	Oct. Fe^{2+}
		0.46	0.50	0.39	15	Oct. Fe^{3+}
38	RT	1.13	2.18	0.32	63	Oct. Fe^{2+}
		1.11	1.88	0.23	22	Oct. Fe^{2+}
		0.45	0.34	0.32	15	Oct. Fe^{3+}
	80 K	1.25	2.70	0.29	40	Oct. Fe^{2+}
		1.25	2.39	0.31	43	Oct. Fe^{2+}
		0.45	0.48	0.40	17	Oct. Fe^{3+}
47	RT	1.17	1.99	0.38	29	Oct. Fe^{2+}
		0.34	0.44	0.35	71	Oct. Fe^{3+}
	80 K	1.28	2.51	0.34	30	Oct. Fe^{2+}
		0.44	0.42	0.38	70	Oct. Fe^{3+}
48	RT	1.16	2.05	0.28	44	Oct. Fe^{2+}
		1.16	1.81	0.28	33	Oct. Fe^{2+}
		0.32	0.54	0.45	23	Oct. Fe^{3+}
	80 K	1.32	2.63	0.37	36	Oct. Fe^{2+}
		1.31	2.25	0.40	45	Oct. Fe^{2+}
		0.26	0.81	0.42	19	Oct. Fe^{3+}
54	RT	1.13	2.11	0.34	100	Oct. Fe^{2+}
	80 K	1.25	2.58	0.31	93	Oct. Fe^{2+}
		0.47	0.69	0.29	7	Oct. Fe^{3+}
58	RT	1.06	1.82	0.33	88	Oct. Fe^{2+}
		0.31	0.27	0.34	12	Oct. Fe^{3+}
	80 K	1.27	2.49	0.32	82	Oct. Fe^{2+}
		0.46	0.50	0.59	18	Oct. Fe^{3+}

Notes: CS = center shift (with respect to α-iron foil); QS = quadrupole splitting; FWHM = full width at half maximum. Estimated uncertainty is ±0.02 mm/s for CS, QS, and FWHM, and ±2% for intensity.

FIGURE 2. Room-temperature (RT) ^{57}Fe Mössbauer spectra of selected axinite samples. Black dots = experimental absorption spectrum; thick line = calculated absorption spectrum; thin lines = Fe^{2+}- and Fe^{3+}-components. Absorption spectra increase in complexity from ferroaxinite (54) to manganaxinite (47).

fortunately the overlap was so large in the Fe^{3+} region that such a hypothesis could not be confirmed nor rejected. However, some Fe^{3+} disorder over two distinct edge-sharing octahedra in samples 26 and 58 is indicated by the cation distribution (Table 7). The Fe^{2+}/Fe^{3+} ratios of samples with intermediate Fe-Mn compositions are close to the ratio of ferroaxinite, with Fe^{2+} ranging from 81 to 89% of total iron. Lastly, the room temperature spectrum of manganaxinite 47 shows weak absorption in the outer part and strong absorption in the inner part, and may be fitted by two doublets (Fig. 2). The outer doublet has CS = 1.17 mm/s and QS = 1.99 mm/s and, according to the previous interpretation, was attributed to Fe^{2+}. The inner doublet shows CS = 0.34 mm/s and QS = 0.44 mm/s and was therefore attributed to Fe^{3+} in octahedral coordination. At liquid nitrogen temperature, no significant differences are observed except for the well known QS increase of the ferrous component. The main difference between this sample and the others is the doublet intensities, which are in this case 30% (Fe^{2+}) and 70% (Fe^{3+}) of total iron. As previously mentioned, this is the first record of Fe^{3+} as the dominant iron species in axinite.

Structural refinement and cation distribution

The results of the site occupancy determination, in agreement with the literature, show that the same cation may be distributed over different sites. As previously mentioned, Mn^{2+} is known to occupy the Ca2 site where is Ca deficient (Basso et al. 1973), and Si may enter the B site (Andreozzi et al. 2000a). Moreover, Fe^{3+} is thought to occupy both Al octahedra (Pieczka and Kraczka 1994; Swinnea et al. 1981; Lumpkin and Ribbe 1979). Thus, to avoid any mismatch between site name and population, as in the structural formulae published so far, the adoption of a more general site nomenclature is recommended. Following the conventions already adopted for complex borosilicates, e.g., tourmalines, the following structural formula is proposed:

$$^{VI}[X1\ X2\ Y\ Z1\ Z2]_2^{IV}[T1\ T2\ T3\ T4\ T5]_2O_{30}(OH)_2$$

in which 10 cationic sites can still be distinguished, but are not directly related to their populations (Table 8). The X1, X2, Y, Z1,

and Z2 octahedral sites may have variable populations and correspond to the former Ca1, Ca2, Fe(Mn), Al1, and Al2, respectively. The T1, T2, T3, and T4 tetrahedral sites correspond to Si1, Si2, Si3, and Si4, respectively, and are totally (or mainly) populated by silicon. Tetrahedral site T5 corresponds to the former B site and is mainly populated by boron, but may host some silicon.

The cell edges and volumes regularly increase from the Fe-richest sample (54) to the Mn end-member (47; Table 3), mainly due to an increase in <Y-O> from 2.220 to 2.255 Å (Fig. 3). The observed <Y-O> increase causes stretching of the edge-sharing Y-Z1-Z2-Z2-Z1-Y octahedral chain in the [211] direction (see Fig. 3 in Andreozzi et al. 2000b). The result is stretching of the cell in the [211] direction (Table 3). The dimensional enlargement of the Y octahedron is geometrically explained by an increase in four out of six bond distances, that is, those with O1, O2, O8, and O10 O atoms. Remarkably, the remaining Y-O6 and Y-O14 bond distances remain almost unchanged, because they were already much longer than the other four. Deformation of the Y octahedron increases with increasing Mn and decreasing Fe, as revealed by the mean square elongation (λ) and angular variance (σ^2) parameters (Robinson et al. 1971), which range from 1.081 to 1.084 and from 220 to 229, respectively. Lower deformation is characteristic of occupancy by smaller cations such as Mg: in fact, in magnesioaxinite, Y distortion decreases to $\lambda = 1.067$ and $\sigma^2 = 178$, because of the predominant reduction of the longest cation-O atom distances (Andreozzi et al. 2000b).

On the basis of experimental results and the minimization procedure (Table 7), substitution of Mn for Fe^{2+} at the Y site is confirmed to be the principal exchange in the axinite-group

TABLE 7. Cation distribution in octahedral sites of axinites and absolute differences between calculated and observed structural parameters

Ax no.	26	30	33	35	38	47	48	54	58
X1 site									
Ca	2.00	2.00	2.00	2.00	2.00	2.00	2.00	1.99	2.00
Total	2.00	2.00	2.00	2.00	2.00	2.00	2.00	2.00§	2.00
Δ_{X1-O} (Å)	0.002	0.002	0.000	0.000	0.001	0.002	0.001	0.001	0.001
$\Delta_{m.a.n.}$	0.51	0.08	0.15	0.25	0.08	0.22	0.14	0.10	0.14
X2 site									
Ca	1.95	1.93	1.90	1.90	1.90	1.90	1.94	1.97	1.92
Mn	0.05	0.07	0.10	0.10	0.10	0.10	0.06	0.03	0.08
Total	2.00	2.00	2.00	2.00	2.00	2.00	2.00	2.00	2.00
Δ_{X2-O} (Å)	0.003	0.004	0.001	0.000	0.002	0.001	0.001	0.004	0.001
$\Delta_{m.a.n.}$	0.60	0.23	0.35	0.28	0.28	0.22	0.42	0.15	0.31
Y site									
Mn	1.03	0.41	1.45	0.74	0.64	1.89	1.33	0.02	1.14
Fe^{2+}	0.83	1.34	0.26	0.85	1.20	0.07	0.62	1.61	0.74
Mg	0.00	0.24	0.28	0.39	0.07	0.01	0.04	0.32	0.05
Zn	0.02	0.00	0.01	0.00	0.00	0.00	0.01	0.01	0.01
Fe^{3+}	0.09	0.00	0.00	0.00	0.04	0.00	0.00	0.02	0.06
Al	0.03	0.01	0.00	0.00	0.05	0.03	0.00	0.02	0.00
Total	2.00	2.00	2.00	2.00†	2.00	2.00	2.00	2.00	2.00
Δ_{Y-O} (Å)	0.000	0.000	0.001	0.001	0.006	0.001	0.002	0.003	0.001
$\Delta_{m.a.n.}$	0.00	0.01	0.03	0.01	0.02	0.02	0.16	0.09	0.02
Z1 site									
Al	1.91	1.86	1.95	1.87	1.85	1.74	1.83	1.92	1.93
Fe^{3+}	0.05	0.14	0.05	0.13	0.15	0.26	0.17	0.08	0.07
Total	2.00*	2.00	2.00	2.00	2.00	2.00	2.00	2.00	2.00
Δ_{Z1-O} (Å)	0.002	0.000	0.003	0.000	0.000	0.001	0.001	0.001	0.001
$\Delta_{m.a.n.}$	0.20	0.00	0.10	0.00	0.02	0.00	0.13	0.20	0.01
Z2 site									
Al	2.00	1.99	2.00	1.97	2.00	1.95	1.98	2.00	2.00
Fe^{3+}	0.00	0.01	0.00	0.03	0.00	0.03	0.02	0.00	0.00
Total	2.00	2.00	2.00	2.00	2.00	2.00‡	2.00	2.00	2.00
Δ_{Z2-O} (Å)	0.001	0.002	0.000	0.000	0.000	0.001	0.001	0.000	0.000
$\Delta_{m.a.n.}$	0.26	0.01	0.17	0.00	0.02	0.00	0.02	0.09	0.13
F(X*i*)	2.0	0.8	1.9	1.4	1.2	1.0	2.0	1.2	1.4

Notes: all values in apfu; F(X*i*) = sum of square residuals divided by number of observed parameters. Empiric cation-oxygen distances used (Å): Ca(X1) = 2.418, Ca(X2) = 2.397, Mn(X2) = 2.307, Mn(Y) = 2.260, Fe^{2+}(Y) = 2.230, Mg(Y) = 2.170, Zn(Y) = 2.180, Fe^{3+}(Y) = 2.090, Al(Y) = 1.970, Al(Z1) = 1.906, Fe^{3+}(Z1) = 2.024, Al(Z2) = 1.900, Fe^{3+}(Z2) = 2.000.
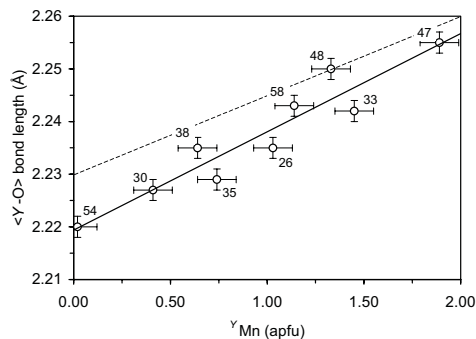* Includes Mg 0.04,
† Includes Ti 0.02,
‡ Includes Mg 0.02,
§ Includes Na 0.01.

FIGURE 3. <Y-O> mean bond-length vs. Mn population at Y site. Solid line = actual trend showing increase in <Y-O> with ^{Y}Mn content. Dashed line = calculated <Y-O> along Fe^{2+}-Mn join. Deviations from calculated trend are due to minor Mg and very minor trivalent cation contents.

TABLE 8. Axinite group minerals: site identification and population

Former name	Revised name	C.N.	Population
Ca1	X1	6	Ca(Na)
Ca2	X2	6	Ca > Mn in axinites, Mn > Ca in tinzenite
Fe(Mn)	Y	6	Mn, Fe^{2+}, Mg in axinites, Mn in tinzenite
Al1	Z1	6	Al, Fe^{3+}
Al2	Z2	6	Al
Si1	T1	4	Si
Si2	T2	4	Si
Si3	T3	4	Si
Si4	T4	4	Si (B)
B	T5	4	B, Si

Note: C.N. = coordination number.

minerals. Most Mn (up to 1.89 apfu) is at the Y site, with the remaining part (up to 0.10 apfu) substituting for Ca at X2, whereas Fe^{2+} is totally ordered at Y. Slight deviations from the strictly linear $^Y Mn^{2+} \leftrightarrow {}^Y Fe^{2+}$ trend (Fig. 4) are due to minor $^Y Mg$ contents and very minor trivalent cation contents (Fe^{3+} up to 0.09 apfu, Al up to 0.05 apfu). These substitutions are responsible for the observed <Y-O> bond distances (Fig. 3), which are shorter than the calculated ones due to the smaller dimensions of Mg, Fe^{3+}, and Al with respect to Fe^{2+} and Mn (Table 7). Remarkably, in spite of the greater abundance of Fe^{2+}-rich samples with respect to Mn- and Mg-rich ones, the ferroaxinite end-member was never observed, either in the literature or in this work.

From ferroaxinite to manganaxinite, the Z1 and Z2 octahedra show an almost regular size increase as a function of <Y-O>. For example, <Z1-O> ranges from 1.910 to 1.921 Å and <Z2-O> from 1.898 to 1.903 Å (Fig. 5). However, the maximum enlargement observed for Z1 is double that observed for Z2. In particular, samples 47 and 48 exhibit a marked increase in <Z1-O> distance and samples 30, 35, and 38 show a less marked but still pronounced increase. The remaining samples show a trend more comparable with that of <Z2-O>.

This behavior is closely related to cation distribution, because Z1 increases in both mean atomic number and dimensions as a function of total Fe^{3+} content, whereas Z2 remains almost unchanged (Figs. 6a, 6b). Accordingly, Fe^{3+} is not equally distrib-

uted between Z1 and Z2, as is usually assumed in the literature, but is strongly ordered at the larger Z1 site. This is in excellent agreement with the cation distribution results (Table 7), and is further evidenced by the close match between observed and calculated <Z1-O> bond distances ($r = 0.93$).

DISCUSSION

Site-occupancy determinations indicate that Fe^{3+} may populate both the Y and Z sites, as was hypothesized based on Mössbauer data. Fe^{3+} at the Y site is rare, it substitutes for divalent cations and is charge-balanced by OH deficiency, according to the general mechanism $^Y M^{3+} + O^{2-} \rightarrow {}^Y M^{2+} + OH^-$. On the contrary, the homovalent substitution $^{Z1} Fe^{3+} \rightarrow {}^{Z1} Al^{3+}$ is more frequent (Fig. 7).

The partial population of Z1 by Fe^{3+} in manganaxinite may be a response to the supergenic conditions in which Mn-rich axinite usually crystallizes (Ozaki 1972), but it is also geometrically favored by structural relationships between Z1 and Y (Fig. 5), because the two octahedra share the O1-O14 edge. Along the Fe-Mn join from ferroaxinite to manganaxinite <Z1-O>, <Y-O>, the O1-O14 distance (+0.020 Å), and the O1-Z1-O14 angle (+0.40°) all increase. This is due not only to the influence of Y (i.e., the second-coordination sphere), but also to the Z1 population, because Fe^{3+} is larger than Al^{3+} (Table 7). Conversely, the limited expansion observed for <Z2-O> is only due to effects of the second-coordination sphere and not to the Z2 population, which is close to pure Al within the whole series (Table 7).

The presence of Fe^{3+} in tetrahedral coordination substituting for B or Si in the axinite-group minerals was proposed for a B- and Si-deficient axinite from Strzegom (Poland) by Pieczka and
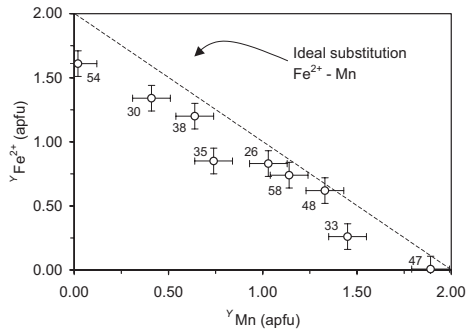
FIGURE 4. Populations of Fe^{2+} vs. Mn at Y site. Solid line represents ideal substitution Fe^{2+}-Mn. Deviations from ideal trend are due to minor Mg and very minor trivalent cation contents.
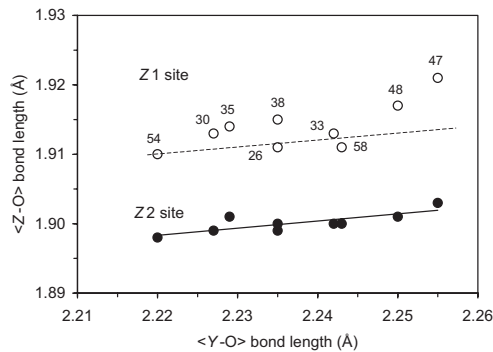
FIGURE 5. Mean bond-lengths <Z1-O> and <Z2-O> vs. <Y-O>. Open circles = Z1 site. Full circles = Z2 site. Symbol size corresponds to about ±1σ of data. Solid line referring to Z2 site is actual linear regression; dashed line is a reference line parallel to previous one.
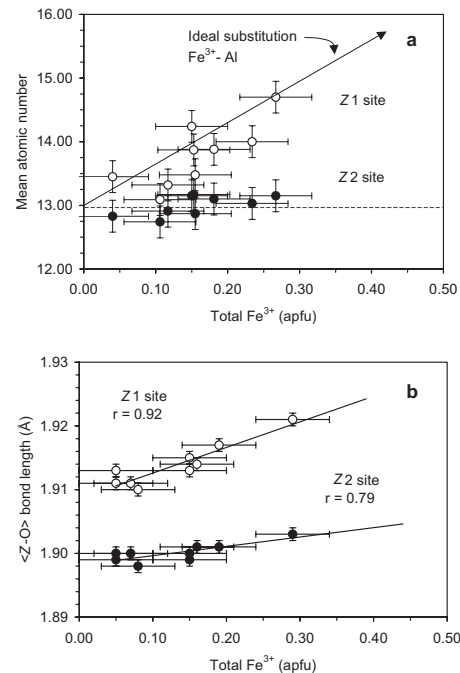
FIGURE 6. Structural parameters of Z1 and Z2 sites vs. total Fe^{3+}. Open circles = Z1 site. Full circles = Z2 site. (**a**) Mean atomic numbers. Solid line = ideal Fe^{3+}-Al substitution; dashed line = Al reference line. (**b**) Mean bond lengths. Solid lines = linear regression.
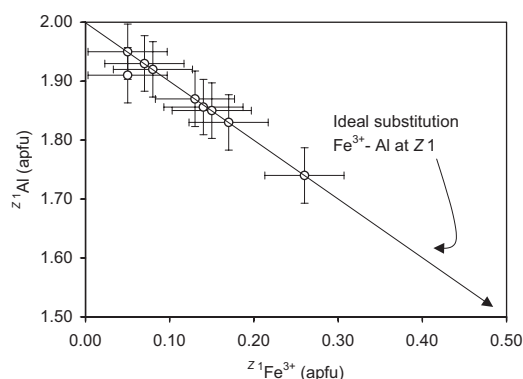
FIGURE 7. Populations of Al vs. Fe^{3+} at Z1 site. Solid line, which represents ideal 1:1 substitution, coincides with linear regression of experimental data ($r = 0.98$).

FIGURE 8. Calculated vs. observed mean bond lengths at T5 site. Open circles = experimental data (most symbols overlap). Solid line = linear regression. Dashed line = calculated $<(B + Si) – O>$ distances. Dotted line = calculated $< (B + Fe^{3+}) – O >$ distances. Ionic radii from Shannon (1976).

Kraczka (1994) on the basis of ^{57}Fe Mössbauer data (CS = 0.14 and QS = 1.60 mm/s), but these data were later partly revised, at least for the $Fe^{3+} \leftrightarrow B$ substitution (Zabinski et al. 2002). Fuchs et al. (1997) claimed to have found Fe^{3+} in tetrahedral coordination in a Norwegian axinite on the basis of their IR results, but their Mössbauer data collected on the same sample showed a CS = 0.4 mm/s that is typical of Fe^{3+} in octahedral coordination (Dyar et al. 1998). Our Mössbauer data (CS ≥ 0.26 mm/s, Table 6) did not suggest the presence of Fe^{3+} in tetrahedral coordination, which is typically evidenced by a CS value of <0.2 mm/s (Dyar et al. 1998). Moreover, in a Mössbauer spectrum of axinite the contribution of Fe^{3+} in tetrahedral coordination cannot be unambiguously distinguished from that in octahedral coordination, due to overlapping Fe^{2+} and Fe^{3+} doublets.

In the case of Fe^{3+} substituting for Si or B, conclusions based on structural data are more reliable, because both T-site mean atomic numbers and <T-O> mean distance have to markedly increase. In our case, all samples show mean atomic number values for the T1-T4 sites very close to 14 and for T5 site close to 5, with none exceeding the reference values for Si and B (Table 4). Moreover, the <T1-O> and <T2-O> values cluster around 1.62 Å, and the <T3-O> and <T4-O> distances around 1.63 Å, which are typical of Si-O bond (Table 3). All of the data, therefore, allow us to exclude the presence of Fe^{3+} at tetrahedrally coordinated sites. Actually, <T5-O> is highest in samples 26 and 35, but this is due to partial substitution by Si rather than Fe^{3+} (Fig. 8). As previously mentioned, in all of the analyzed samples the B+Si sum was enough to fill the tetrahedral sites (Andreozzi et al. 2000a).

The case in which excess B (>2 apfu) substitutes for Si was only observed as a very minor substitution in two samples (30 and 54). However, the small extent of B → Si substitution observed is not clearly reflected by changes in structural parameters: this makes it difficult to judge whether or not it occurs, and what the charge-balance compensation mechanism is. If the B → Si substitution were observed elsewhere in higher proportions, it could be added as a general mechanism for the axinite mineral group. From structural considerations, this substitution may occur at the T4 tetrahedron, the most external of the $[B_2Si_8O_{30}]$ planar cluster, and the only one not directly linked to a B-centered tetrahedron.
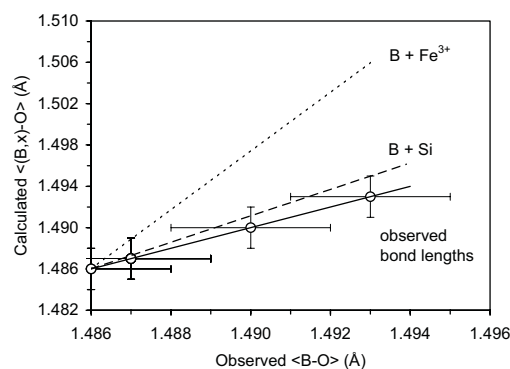
The *Y* octahedron guides almost all structural deformations in axinite. Because of its central position and variable occupancy, *Y* deformations lead variations with respect to cell edges, angles, and volume. The *Z1* octahedron is larger than *Z2*, and both sites expand as a function of <*Y*-O>, which in turn depends on Mn content. These relationships explain why the substitution of Fe^{3+} for Al occurs only in *Z1* and is favored toward Mn-rich samples.

Axinite is confirmed to be a group name, with specific names for the four end-members (manganaxinite, ferroaxinite, magnesioaxinite, tinzenite), defined by both chemistry and cation ordering. In our samples, the populations of Zn, Al, and Fe^{3+} at *Y* site were very limited, but Fe^{3+} reached 13% of site occupancy at *Z1* site, and the occurrence of samples with highest Fe^{3+} cannot be excluded. For these samples the adoption of new names with ferri- as a prefix would be required (ferri-manganaxinite, ferri-ferroaxinite).

REFERENCES CITED

Andreozzi, G.B. (1997) Crystal chemistry of axinites, Ph.D. dissertation, 208 pp. University of Rome "La Sapienza". Rome and Florence National Libraries, Earth Science Section.

Andreozzi, G.B., Ottolini, L., Lucchesi, S., Graziani, G., and Russo, U. (2000a) Crystal chemistry of the axinite-group minerals: A multi-analytical approach. American Mineralogist, 85, 698–706.

Andreozzi, G.B., Lucchesi, S., and Graziani, G. (2000b) Structural study of magnesioaxinite and its crystal-chemical relations with axinite-group minerals. European Journal of Mineralogy, 12, 1185–1194.

Basso, R., Della Giusta, A., and Vlaic, G. (1973) La struttura della tinzenite. Periodico di Mineralogia, 42, 369–379.

Belokoneva, E.L., Pletnev, P.A., and Spiridonov, E.M. (1997) Crystal structure of low-manganese tinzenite (severginite). Crystallographic Reports, 42, 1010–1013.

Bosi, F. and Lucchesi, S. (2004) Crystal chemistry of the schorl-dravite series. European Journal of Mineralogy, 16, 335–344.

Burnham, C.W. (1990) The ionic model: Perceptions and realities in mineralogy. American Mineralogist, 75, 443–463.

Deer, W.A., Howie, R.A., and Zussmann, J. (1986) Rock-Forming Minerals. Disilicates and Ring Silicates: Axinite, vol. 1B, second ed. Longmans, Green and Co., London.

Dyar, M.D., Taylor, M.E., Lutz, T.M., Francis, C.A., Guidotti, C.V., and Wise, M. (1998) Inclusive chemical characterization of tourmaline: Mössbauer study of Fe valence and site occupancy. American Mineralogist, 83, 848–864.

Eeckhout, S.G. and De Grave, E. (2003) Evaluation of ferrous and ferric Mössbauer fractions. Part II. Physics and Chemistry of Minerals, 30, 142–146.

Fuchs, Y., Linares, J., and Robert, J.L. (1997) Mössbauer and FTIR characterization of a ferro-axinite. Hyperfine Interactions, 108, 527–533.

Grew, E.S. (1996) Borosilicates (exclusive of tourmaline) and boron in rock-forming minerals in metamorphic environments. In L.M. Anovitz and E.S. Grew, Eds., Boron: Mineralogy, Petrology, and Geochemistry, 33, 387–502. Reviews in Mineralogy, Mineralogical Society of America, Washington, D.C.

James, F. and Roos, M. (1975) MINUIT. A system for function minimization and analysis of the parameters errors and correlations. Computer Physics Communications, 10, 343–367.

Lavina, B., Salviulo, G., and Della Giusta, A. (2002) Cation distribution and structure modelling of spinel solid solutions. Physics and Chemistry of Minerals, 29, 10–18.

Lumpkin, G.R. and Ribbe, P.H. (1979) Chemistry and physical properties of axinites. American Mineralogist, 64, 635–645.

Ottolini, L., Bottazzi, P., and Vannucci, R. (1993) Quantification of lithium, beryllium, and boron in silicates by secondary ion mass spectrometry using conventional energy filtering. Analytical Chemistry, 65, 15, 1960–1968.

Ottolini, L., Bottazzi, P., and Zanetti, A. (1995) Determination of hydrogen in silicates by secondary ion mass spectrometry. Analyst, 120, 1309–1313.

Ozaki, M. (1972) Chemical composition and occurrence of axinite. Kumamoto Journal of Science, Geology, 9, 1–34.

Pieczka, A. and Kraczka, J. (1994) Crystal chemistry of Fe^{2+}-axinite from Strzegom. Mineralogica Polonica, 25, 43–49.

Pringle, I.J. and Kawachi, Y. (1980) Axinite mineral group in low-grade regionally metamorphosed rocks in southern New Zealand. American Mineralogist, 65, 1119–1129.

Robinson, K., Gibbs, G.V., and Ribbe, P.H. (1971) Quadratic elongation: a quantitative measure of distortion in coordination polyhedra. Science, 172, 567–570.

Sanero, E. and Gottardi, G. (1968) Nomenclature and crystal chemistry of axinites. American Mineralogist, 53, 1407–1411.

Shannon, R.D. (1976) Revised effective ionic radii and systematic studies of interatomic distances in halides and chalcogenides. Acta Crystallographica, A32, 751–767.

Swinnea, J.S., Steinfink, H., Rendon-Diaz Miron, L.E., and Enciso de La Vega, S. (1981) The crystal structure of a Mexican axinite. American Mineralogist, 66, 428–431.

Takéuchi, Y., Ozawa, Y., Ito, T., Araki, T., Zoltai, T., and Finney, J.J. (1974) The $B_2Si_8O_{30}$ groups of tetrahedra in axinite and comments on deformation of Si tetrahedra in silicates. Zeitschrift für Kristallographie, 140, 289–312.

Zabinski, W., Pieczka, A., and Kraczka, J. (2002) A Mössbauer study of two axinites from Poland. Mineralogica Polonica, 33, 27–33.